Understanding Pharmaceutical Flows

Joseph Kukura, Paulo Campos Arratia, Edit S. Szalai, Kevin J. Bittorf, and Fernando J. Muzzio*

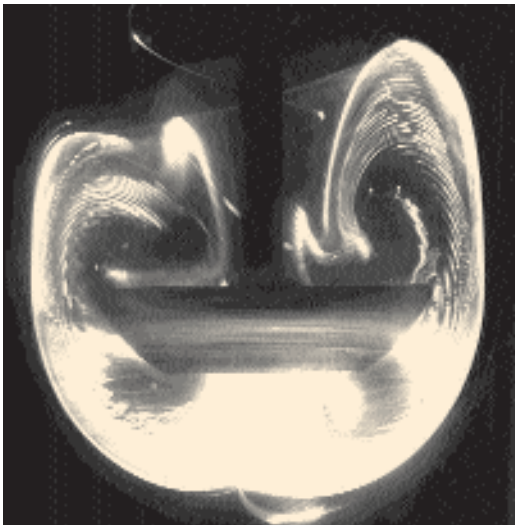

FERNANDO J. MUZZIO

The combined use of experimental fluid dynamics (EFD) and computational fluid dynamics (CFD) methods effectively identifies and addresses flow problems in the pharmaceutical industry. Process performance and reliability can be improved with the application of this technology. This article demonstrates the use of EFD/CFD with diverse examples, including a laboratory dissolution apparatus, stirred tanks in various configurations, mixing of non-Newtonian fluids, static mixers, and roller bottles. Flow patterns, mixing structures, and complex behavior are all revealed with the combination of EFD and CFD methods.

Joseph Kukura is a graduate student, Paulo Campos Arratia is a graduate student, and Edit S. Szalai is a graduate student at the Department of Chemical and Biochemical Engineering of Rutgers University. Kevin J. Bittorf, PhD, is a CFD applications engineer at Dantec Dynamics (Mahwah, NJ), and Fernando J. Muzzio, PhD, is professor and director of the pharmaceutical engineering program at the Department of Chemical and Biochemical Engineering of Rutgers University, 98 Brett Road, Piscataway, NJ 08854-8058, tel. 732.445.3357, muzzio@sol.rutgers.edu.

*To whom all correspondence should be addressed.

Fluid flow is an important aspect in various pharmaceutical industry processes, including large production-scale equipment applications, flows in laboratory devices used to analyze and develop drugs, and biological transport in the human body. To improve the development, production, analysis, and delivery of new therapies, efficient tools are needed to characterize, understand, and ultimately predict flow in relevant systems. Several factors motivate improved understanding of these flows. Ever more complex synthesis of drugs, tighter regulatory requirements, and the development of novel drug delivery systems involve increasingly sophisticated fluid flow. Fluid motion can affect several steps needed to produce a pharmaceutical product, thus highlighting the need to advance the study of fluid flows throughout the industry.

The most effective and meaningful approach to study flow fields combines both experimental and computational techniques. The rapid advancement of computing power during the past few years has led members of software companies and chemical industry consultants to report computational fluid dynamics (CFD) as a viable tool for understanding many processes (1,2). However, those articles focused on the role of CFD in studying flows without significant reference to the complementary experimental validation. The output of CFD is entirely dependent on the suitability of physical models and pa-

rameters used for the simulations, and the accuracy of the results can be evaluated only with experimental information. Experimental fluid dynamics (EFD) not only determines whether appropriate models and parameters are used in CFD simulations but also provides meaningful insights regarding the physics of fluid flows. With balanced support and input from EFD, CFD can be used with confidence to rapidly obtain information that is difficult to obtain experimentally. The combined techniques have been applied extensively to traditional engineering applications such as scale-up and equipment design. Other areas such as biological synthesis, tablet dissolution performance, and human pulmonary flows also have been studied using experimental and computational techniques (3–5).

This article demonstrates the use of the combination of EFD and CFD to study fluid flow in several situations. A collection of experimental techniques, including acid–base flow visualization, UV fluorescence, planar laser induced fluorescence (PLIF), and particle image velocimetry (PIV), combined with CFD, are applied to flows in pharmaceutical equipment. The approach of using both experimental and computational tools described in this article can expand scientific insight and improve data collection, equipment design, and process optimization and scale-up. The examples include systems that are traditionally within the realm of engineering study as well as devices that historically have been out of the hands of engineers. The first example illustrates in great detail the use of CFD and EFD in a study of a dissolution apparatus used for analytical testing and validation. Because stirred tanks are used in many areas of the pharmaceutical industry, two tank examples are presented. Analysis of a static mixer used in applications such as liquid formulation processing follows the tank section, and the final example evaluates flow in roller bottles used for biological processes.

Experimental and computational techniques

Many approaches for measuring fluid flow and mixing provide valuable information about bulk properties but fail to describe the details of fluid motion. A common method for analyzing flows in reactors involves measuring residence time distribution (RTD) (6,7). This convenient method for evaluating macromixing does not provide the complete two-dimensional or three-dimensional flow structures or mixing information, and the fact that a variety of flow patterns can produce the same RTD is a limitation.

Experiments using fast competing reactions can indirectly provide an average measure of micromixing by quantifying selectivity of the reactions (8–11). However, the hydrodynamic environment varies significantly from one mixer to another, and local effects are missed entirely. When more-detailed information about flow systems is required, flow visualization and computational methods must be used.

Use of PIV. A powerful tool for obtaining quantitative velocity field information is particle imaging velocimetry, which has been applied to several industrial flow systems (12). This nonintrusive technique measures a two-dimensional velocity field at a given plane illuminated by a laser sheet after the experimental fluid has been seeded with neutrally buoyant reflective particles. These particles follow the same trajectories as the fluid molecules and reflect the laser light. A digital camera is used to capture images of the illuminated plane. The particles located in the plane appear as bright points against a dark background in such images. Two successive snapshots of the illuminated plane are required to calculate the two-dimensional velocity field using a fast-Fourier transforms (FFT) cross-correlation algorithm. The quantitative measurements from PIV can be compared statistically and visually to computational calculations at fixed locations. In the study described in this article, the authors used a Dantec PIV system (Dantec Dynamics, Mahwah, NJ) to calculate the velocity fields.

Use of PLIF. In addition to measuring velocity fields, experimental techniques can reveal the motion of tracers moving in the flow. Carefully conducted dye advection experiments unveil flow patterns and structures that serve as the starting point to analyze fluid mixing. Dye advection experiments use a neutrally buoyant dye to avoid disrupting the flow. In the present study, the authors used fluorescent dyes illuminated with a UV lamp to show three-dimensional mixing structures. Convection carries dye rapidly to regions where mixing is good, while segregated regions of the mixer remain dark for a long period of time. These simple experiments are useful for identifying segregated and well-mixed regions. However, they cannot reveal detailed flow structures within the regions because the images from these experiments are two-dimensional projections of three-dimensional fields. Visualization of the internal flow structures can be performed by illuminating the fluorescent dye with a planar laser sheet. PLIF is used to reveal mixing patterns at specific two-dimensional planes. For the images reported in this article, a 32 mJ Nd:YAG laser (New Wave Research, Sunnyvale, CA) generated the laser sheet with a wavelength of 532 nm. Images were captured using a Dantec 80C42 double-image 700 CCD camera (Dantec Dynamics) with a 552-nm filter. Structures revealed with this technique are readily compared with patterns identified by tracking particles in computational flow fields. In addition to observing qualitatively how the dye distributes, the intensity of the emitted light can be correlated to the dye concentration in each region of the mixer to quantify homogeneity (13,14).

Developing a CFD model. CFD is implemented to obtain data that are difficult to obtain experimentally and to develop effective models for scale-up and optimization. The first step of CFD modeling is to create a geometrical representation of the flow region. A mesh of this region subsequently is built to define the locations where an algebraic form of the relevant governing conservation equations are solved. For fluid flow, the governing equations always include mass and momentum conservation for either laminar or turbulent conditions and may require energy conservation for nonisothermal systems and/or chemical species transport equations for multicomponent systems. The selection of models and parameters used in these computational methods are based on experimental data. The computational solver obtains solutions for the flow variables at as many as several million locations, as defined by the mesh. Details of the solution techniques are abundant in the literature (15–17).

After the solver generates velocity, pressure, and other data for the entire flow field, the information is used in postprocessing steps. Postprocessing analysis ranges from visualization of the computed variables, to calculating integrated quantities such as heat transfer rates, to quantifying the dispersion of initially segregated particles. The simulated velocity fields for the dissolution apparatus, stirred tanks, and static mixer examples in this article were generated using the ORCA CFD package (Dantec Dynamics). The velocity fields for the roller bottle examples were created using the Fluent CFD package (Fluent Inc., Lebanon, NH). Custom software developed at Rutgers University was used for postprocessing analysis.

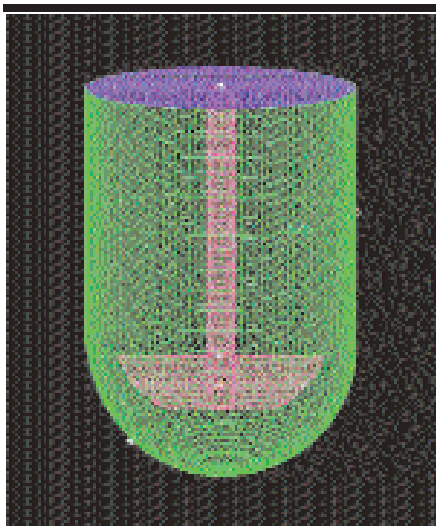

Figure 1: Diagram of USP Apparatus II.

Applications of EFD and CFD

Dissolution apparatus. An excellent example of a pharmaceutical flow that has so far escaped engineering analysis is the dissolution apparatus. This device has been largely studied and used by chemists, pharmacists, and quality control professionals (18). Hydrodynamics have been shown to influence dissolution testing performance for several decades (19–21). However, most studies involving this apparatus correlated changing conditions to concentration measurements and did not study the underlying flow conditions (22–24). Case-by-case performance evaluations have been carried out, but a general characterization that helps a priori design is still lacking. As alternative dissolution apparatus configurations and operating conditions are being considered (such as smaller devices and slower agitation speeds), a detailed analysis of the flow in this system should be performed to implement select changes rationally based on fundamental principles. The need for this analysis is evident from work that measured velocities at selected locations and identified recirculating flow in the USP Apparatus II, which is one of the most commonly used dissolution testing devices (5). Visualization studies with dye released from a nondisintegrating tablet showed that shear patterns can be unstable across the surface of a pill in the same device, possibly leading to inconsistent performance (25).

The USP Apparatus II has been studied using both experimental and computational techniques (26). A diagram of the apparatus is shown in Figure 1. The figure shows the outline of the geometry and surface mesh used in CFD calculations. Figures 2 and 3 show PIV velocity field measurements at two agitator speeds in the apparatus. Each figure contains two velocity fields measured at small time intervals at a vertical plane adjacent to the shaft in the center of the device. Flow in stirred devices such as this apparatus are typically characterized with a dimensionless Reynolds number (*Re*) calculated as follows:

$$Re = \rho N D^2 \div \mu \qquad [1]$$

in which ρ is the fluid density, μ is the fluid viscosity, N is the rotational speed of the agitator, and D is the diameter of the agitator.

The behavior of the flow field in a stirred mixer is a function of only the Reynolds number during isothermal operation for a given geometrical shape provided there is no significant vortex. The two velocity fields in Figure 2 were taken at short time intervals for $Re = 5000$, which corresponds to standard operating conditions. In this figure, and in the remainder of this article, blue represents low velocities and red corresponds to high velocities. The flow is distinctly asymmetric, and the velocity field changes significantly in the small time interval between Figures 2a and 2b. The figures show that the locations of large recirculating loops changed quickly. These large recirculating eddies are of the same size scale of small tablets, and their inconsistent behavior could easily affect the consistency of dissolution measurements with uneven transport of material through the device. The images indicate that the flow is in a regime of transitional turbulence. Unlike fully turbulent

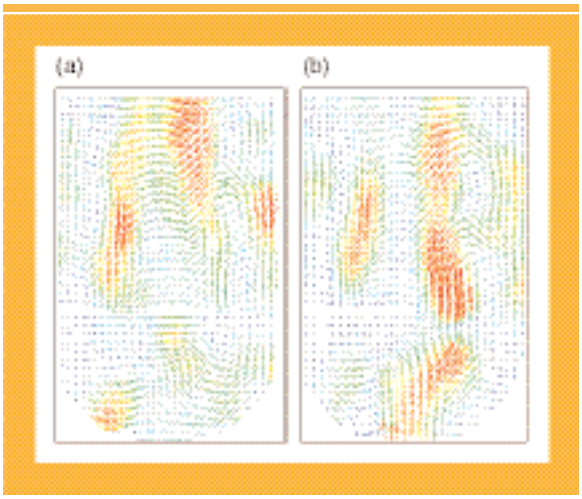

Figure 2: Two PIV velocity-field measurements in USP Apparatus II at $Re = 5000$ taken with short time intervals between measurements.

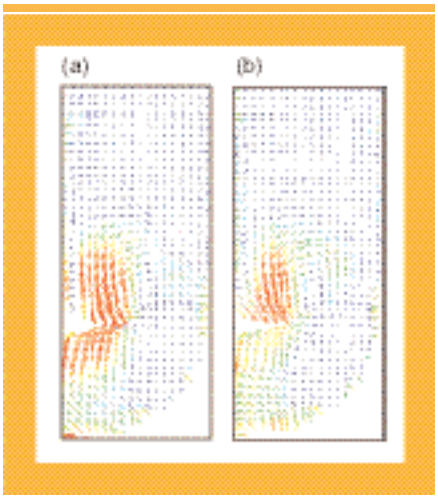

Figure 3: PIV velocity-field measurements in USP Apparatus II at $Re = 100$ taken with short time intervals between measurements.

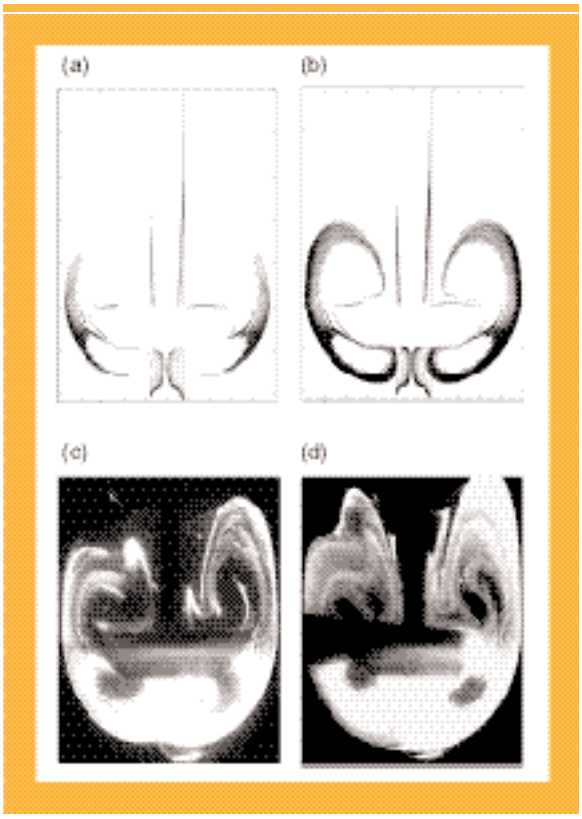

Figure 4: (a and b) Numerical and (c and d) PLIF flow structures in USP Apparatus II at $Re = 100$.

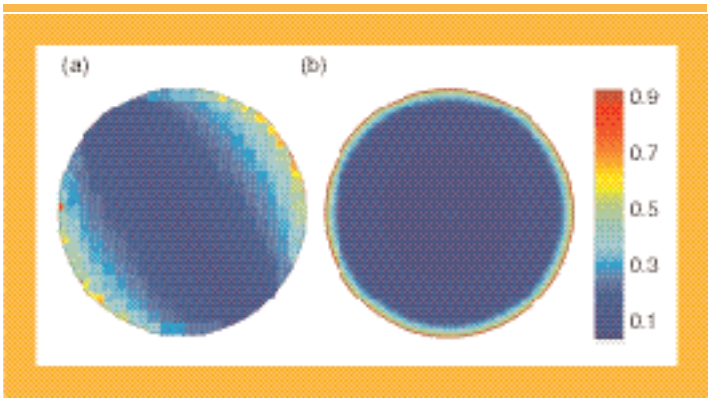

Figure 5: Strain-rate contours on the top surface of a tablet at the bottom of a USP Apparatus II on an (a) instantaneous and (b) time-averaged basis.

flows, which are steady on a time-averaged basis, flows in transitional turbulence often vary on a measurable time scale that leads to process inconsistency. Identification of such flow regimes is an important component of the experimental study of pharmaceutical flows.

In contrast with the unsteady behavior shown in Figure 2, the PIV velocity fields shown in Figure 3 were measured at $Re = 100$, which represents operation in smaller vessels or the use of slower agitation speeds. Only half of the velocity field is shown in each image because the flows are completely symmetric. The left side of the images corresponds to the center of the vessel, and the right side corresponds to the wall. The small variations from one image to the next indicate that the flow is in a steady, laminar regime. Two recirculating regions in areas just above and below the impeller, which have been observed in other stirred vessels operated in the laminar regime, indicate possible segregation in the flow (27).

At the present time, CFD is especially well suited for simulating the steady flow shown in Figure 3. A steady CFD simulation for $Re = 100$ was performed for the USP Apparatus II with a small cylindrical tablet located at the bottom of the apparatus. The experiment used an unstructured tetrahedral mesh with 1.8 million volumetric elements. After the steady state velocity field was generated using CFD, an analysis of mixing performance was undertaken. While velocity fields indicate long-term recirculation zones in the flow and possible isolated zones, they are not adequate to describe mixing dynamics. Short-term heterogeneities and long-term segregated regions, which can be a primary source of inconsistent behavior, are revealed by Lagrangian analysis of fluid motion. In a Lagrangian analysis, flow patterns and coherent structures are generated by tracking passive particles in the flow to analyze fluid mixing. Progress of the mixing process is assessed by examining the location of tracers as a function of space and time.

The computational velocity field for $Re = 100$ was used for simulations that tracked particles in the USP Apparatus II. The particles, which were initially placed in a vertical line near the shaft in the plane perpendicular to the paddle, revealed flow structures above and below the agitator. Whenever a particle moved through the cross section parallel to the agitator blade at the center of the vessel, its position in the plane was recorded. Plotting the particle positions for various times reveals the mixing structure in the vessel (see Figure 4). Figure 4a corresponds to the intersections recorded during 10 impeller revolutions, and Figure 4b contains the results for 20 revolutions. After 10 impeller revolutions, the dye was ejected from the impeller toward the vessel wall. A complex, layered mixing pattern near the paddle was revealed after a period of time. After 20 revolutions, more details of the mixing pattern appeared. The fluid wrapped around the impeller toward the shaft and outlined the slow mixing regions above and below the blade. None of the dye actually went into the top region of the vessel unless it was originally injected there. The heterogeneous pattern persisted for a long period of time. This behavior has significant implications regarding the most suitable location and method for obtaining samples from the tank. Samples taken from segregated zones will not be representative of the majority of the fluid in the device.

The mixing patterns identified in Figures 4a and 4b were validated using PLIF experiments. Figures 4c and 4d show images from a PLIF experiment conducted in a standard USP Apparatus II under laminar-flow conditions. The dye was initially injected at the bottom of the vessel (as if released from a tablet located there), and the laser plane was projected through the center of the tank when the paddle was in the plane. The structures identified in the simulation match the experimental images. The dark regions in Figures 4c and 4d correspond to locations where dye will not be transported by convection. Particles do not penetrate these areas in either the simulations or the ex-

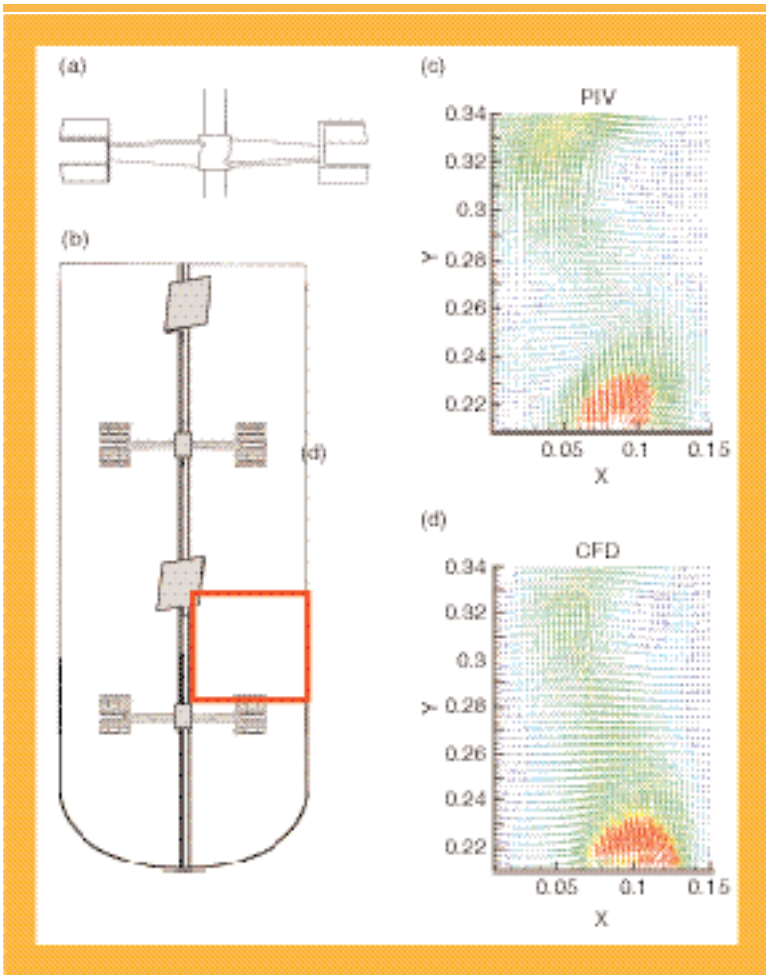

Figure 6: (a) Intermig impeller diagram, (b) tank schematic, and (c and d) PIV and CFD velocity-field measurements.

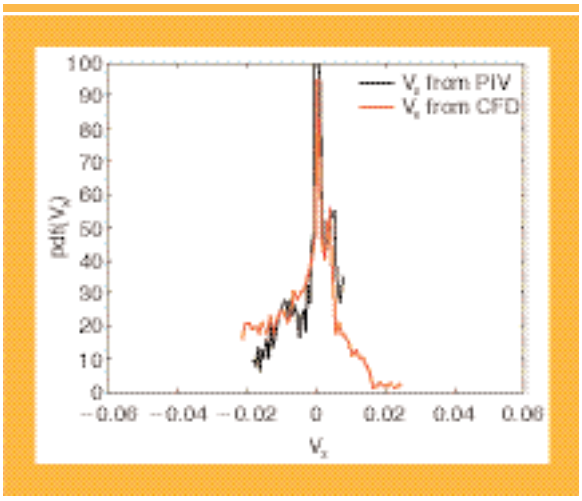

Figure 7: Validation of CFD radial velocity with PIV data.

periments. The edges of these dead zones have a consistent folding pattern during both simulation and experimentation. Similarity of mixing patterns in the computational and experimental systems indicates that the fundamental mechanisms of fluid motion and mixing are being accurately captured in the simulations. Following this validation of the models, variations in vessel design and operating conditions can be evaluated with confidence using CFD.

Validated CFD models are especially powerful for obtaining information that is difficult to characterize and quantify experimentally. One example is obtaining the shear field on the surface of a tablet in a USP Apparatus II. The velocity field used to generate Figures 4a and 4b was used to quantify the strain that is exerted on the surface of a cylindrical pill located at the bottom of a USP Apparatus II. Figure 5a shows an instantaneous calculation, and Figure 5b shows time-averaged values. Low values are depicted in blue, and high values are shown in red. The highest values of the strain rate are exerted at the edge of the pill, which may not correspond well to stress distribution on a tablet in the body and which may hinder meaningful evaluation of tablet dissolution performance.

In summary, CFD and EFD offers a powerful combination for the analysis of flow and mixing in a USP Apparatus II. A rational design of hydrodynamic effects on dissolution testing can be evaluated with a combination of the experimental and computational approaches described in this article.

Stirred tanks

The techniques discussed in the previous example for a laboratory-scale dissolution apparatus also are suitable for large-scale production equipment. Stirred tanks are among the most common equipment used for processing in the pharmaceutical industry because of their versatility. These units provide flexibility to make many high-value, low-volume products by serving diverse roles, including reactors, mixers, extractors, fermenters, crystallizers, distillation pots, and suspension devices. Because process scale-up in stirred tanks for these operations has been a focus of the engineering community for a long time, many examples of applying CFD and EFD to understand fluid flow are available in various configurations. This section presents two examples that have distinct pharmaceutical relevance: a tank with Intermig (Ekato Corp., Ramsey, NJ) impellers for low-shear applications and the mixing of an inelastic shear-thinning fluid in a stirred tank.

Tank with impellers. The blades of Ekato Intermig impellers have opposing pitches within each blade (see Figure 6a). The impellers often are installed in pairs, with each impeller perpendicular to the one above or below it. Figure 6b depicts the tank with four impellers used in the authors' study. These agitators are commonly used for processes that require thorough axial mixing with minimal shear such as fermentations that use cells that are easily destroyed by intense agitation or crystallization of shear-sensitive crystals. The laboratory tank used for our experimental and computational study had a radius of 15.24 cm and height of 82.88 cm with equally spaced impellers of radius 10.67 cm.

High-resolution PIV images that included the entire height of the vessel were difficult to obtain with a tank of this size, so

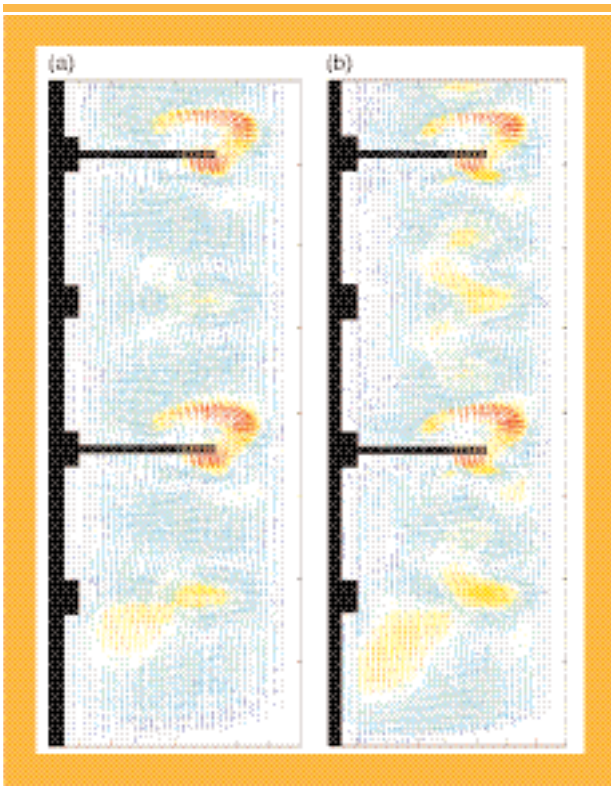

Figure 8: Velocity field in a tank with four Intermig impellers at (a) *Re* = 50 and (b) *Re* = 100.

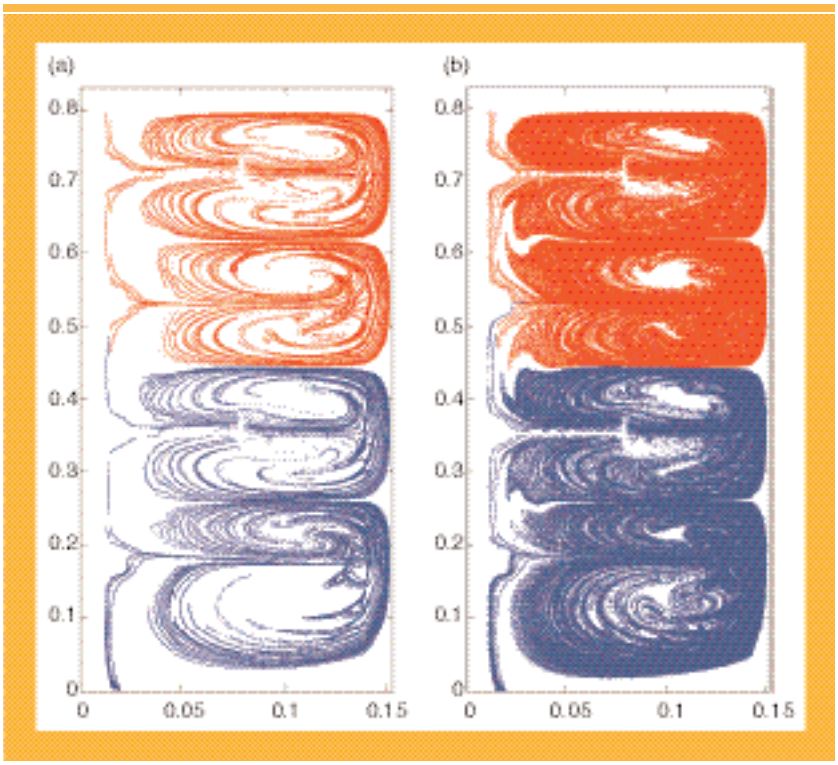

Figure 9: Particle tracking in a tank with four Intermig impellers after (a) 10 and (b) 20 revolutions showing segregation patterns at *Re* = 50.

data were collected in multiple smaller sections. The red box in Figure 6b shows an example of a section. The experimental and computational velocity fields in this region are shown for *Re* = 37 in Figures 6c and 6d, respectively. The *x*-axis in these figures corresponds to one arm of the bottom impeller, and the shaft runs along the *y*-axis. The qualitative comparison of the experimental and computational velocity fields was very good. An *S*-shaped flow moves upward from the impeller at the bottom of the field. A recirculating zone also was found near the top-right corner of both velocity fields, thereby providing an indication of segregation in the flow.

The CFD and EFD velocity fields had excellent quantitative agreement. Figure 7 shows the probability density functions of the radial component of velocity for the PIV and CFD images in Figure 6c and 6d. Satisfying correspondence was observed. Velocity data for the axial direction and velocities in other regions also matched well.

Full-velocity fields for half of the tank from the validated CFD model are shown in Figures 8a and 8b for *Re* = 50 and *Re* = 100, respectively. As the authors discussed in the previous example of a dissolution apparatus, a velocity field does not provide complete dynamic information, and postprocessing work must be performed to understand mixing patterns. Next, Lagrangian techniques were applied to this complex geometry to study axial mixing and flow structures in the tank. Particles were injected in a line near the shaft and tracked in a steady-state flow simulation. Figure 9 shows how the intersections of these particles in a plane were plotted after 10 (a) and 20 (b) revolutions in a flow with *Re* = 50. Particles injected at the top half of the tank are colored red, and particles injected on the bottom half are colored blue. The results of the particle tracking show two important features: Segregated structures form in the flow, and axial mixing between the top half and bottom half of the tank is slow. These features are not obvious from the velocity fields shown in Figure 8, thus demonstrating the need for Lagrangian postprocessing analysis.

Experimental validation of both small-scale and large-scale flow features is available. Figure 10 shows enlarged images of the segregated regions from a PLIF experiment and CFD particle tracking. The top of each image corresponds to a height where an impeller (second from the bottom) is located, and the bottom of the figures is at a height between the lowest impeller and the one above it. The segregated region is black in the experimental image of Figure 10a. The same dead zone appears in white in the computational pattern of Figure 10b. The folds in each impeller region are created as the impeller folds fluid elements and then pushes them toward the vessel wall. Convection never brings dye tracers into these regions under these conditions.

Figure 11a confirms the larger scale mixing issue by showing images from an acid–base visualization experiment. The experiment started with an initially basic solution containing a pH indicator that changes from blue to yellow as the mixture becomes acidic. A charge of concen-

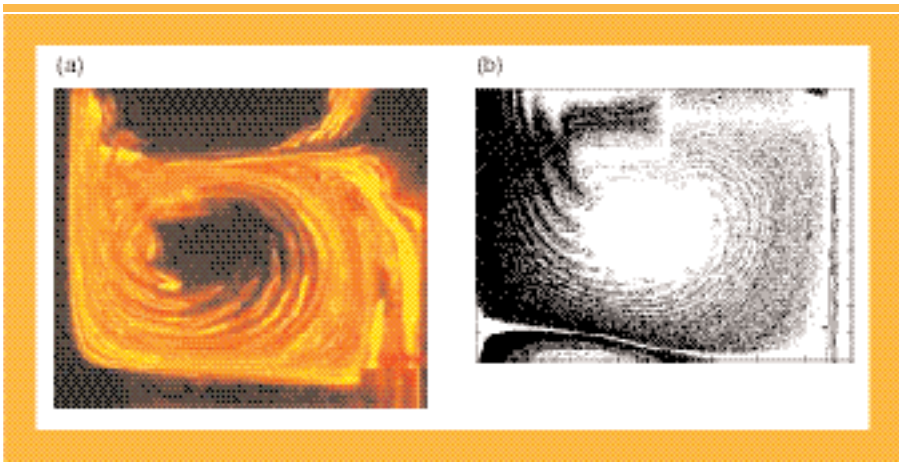

Figure 10: Comparison of (a) PLIF and (b) CFD flow structures below an Intermig impeller.

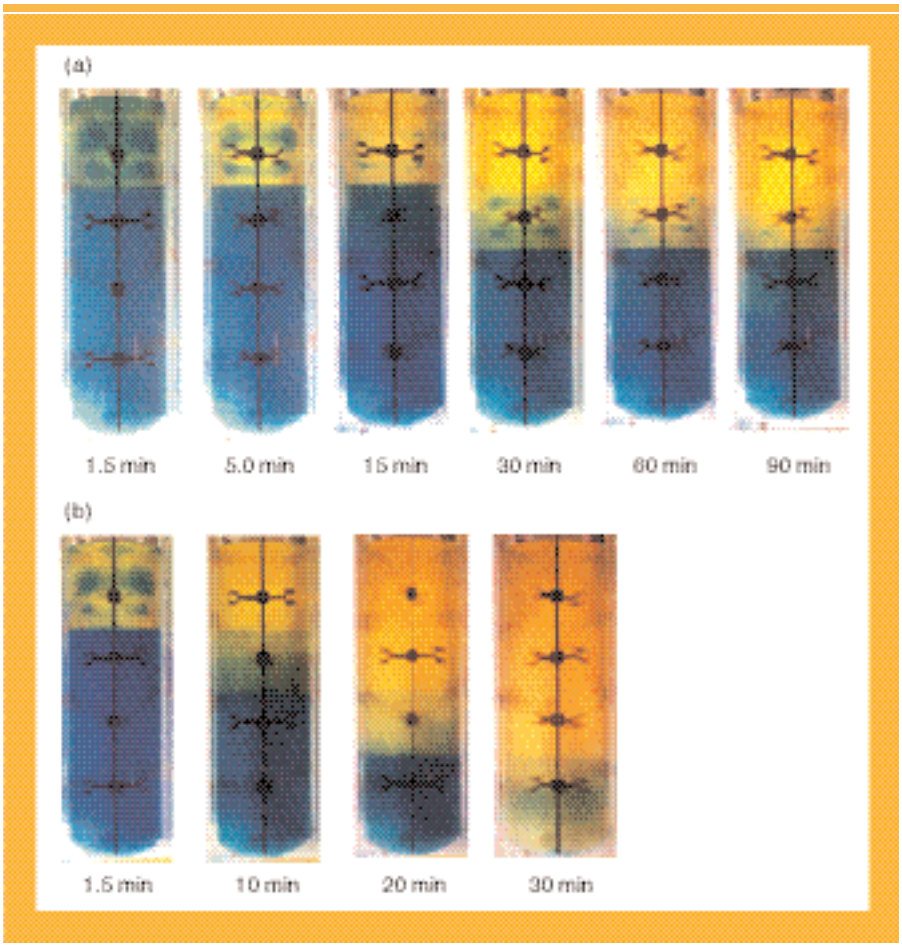

Figure 11: Mixing comparison with an acid–base experiment using (a) constant agitation speed and (b) variable agitation speed.

trated acid was added at the top of the tank, and pictures were taken at regular time intervals to show the progression of the axial mixing. The photographs, in time sequence, are shown in Figure 11a, where the fluid in the top half of the tank became yellow relatively rapidly (≤30 min), but the bottom half of the tank remained segregated from the acid in the top half of the tank for an extended time (>90 min). Eliminating this type of segregation with variable agitator speeds has been demonstrated experimentally and computationally in other systems (27,28). This technique was applied to the tank with Intermig impellers shown in Figure 11b using equivalent conditions to the experiment of Figure 11a, except the agitation speed was varied between $Re = 37$ and $Re = 74$ every 1 min. A comparison of Figures 11a and 11b clearly shows that the fluid traveled more efficiently between the top and bottom of the tank with the use of variable agitation speed. Additional details that describe mixing in this tank are reported elsewhere (29).

Mixing non-Newtonian fluids in a tank

The processing of many pharmaceutical products involves non-Newtonian fluids. Xanthum gum and Carbopol (Noveon, Cleveland, OH) are two common additives that cause a fluid to have shear-thinning properties. These fluids have unique mixing properties that have been studied extensively in experiments (30–33). When yield-stress shear-thinning fluids are mixed in stirred tanks, a well-known phenomenon that occurs is the formation of well-mixed zones around the impellers while the remainder of the fluid remains relatively stagnant. These well-mixed zones, commonly known as *caverns,* have been characterized for various impellers (34). Figure 12 shows experimental images of caverns in a tank mixed with three equally spaced Rushton impellers moving at 50, 150, and 300 rpm. The fluid in the tank is 0.1% Carbopol in an aqueous solution. Fluorescent dye was injected close to each impeller, and the pictures were taken after dye penetrated the entire cavern regions. After green dye was injected near the middle impeller and red dye was injected near the upper and lower impellers, the experiments showed that the caverns did not mix with each other even when they were in direct contact at an impeller speed of 300 rpm.

A CFD model of this system was used to investigate mixing behavior within and around the caverns. The simulations use a bounded viscosity model that fits the rheological data. Figure 13 shows velocity contours from the CFD simulations at 50, 150, and 300 rpm that compare well with PIV experimental measures (not shown in the interest of brevity). This figure

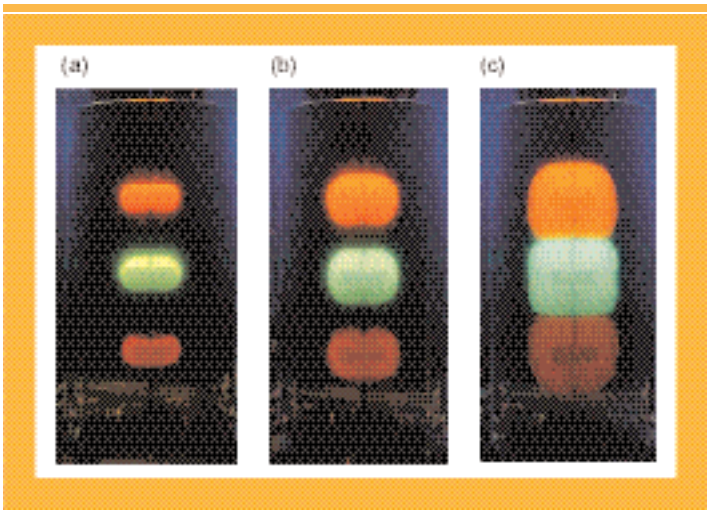

Figure 12: UV fluorescence experiments identifying the growth of caverns in a tank mixing 0.1% Carbopol using three Rushton impellers at (a) 50 rpm, (b) 150 rpm, and (c) 300 rpm.

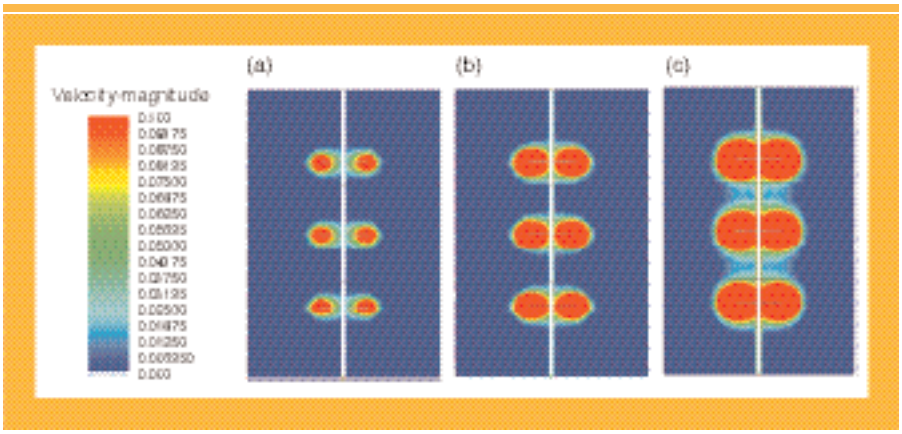

Figure 13: Velocity magnitude contours in a simulated tank mixing 0.1% Carbopol using three Rushton impellers at (a) 50 rpm, (b) 150 rpm, and (c) 300 rpm.

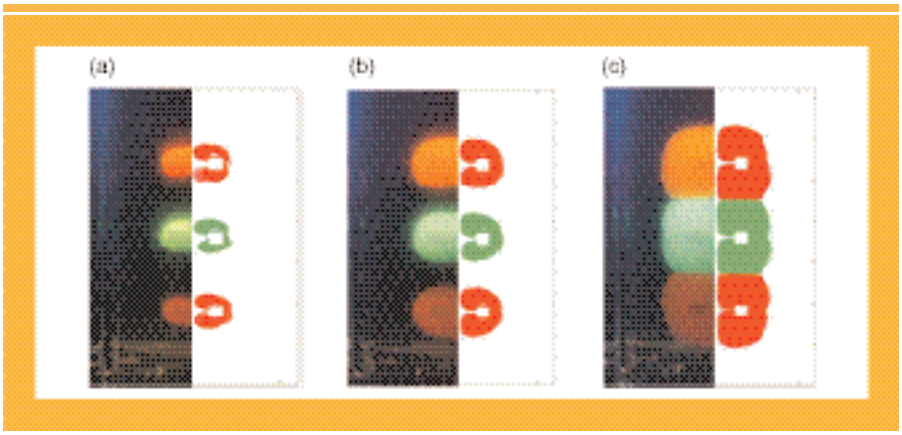

Figure 14: Comparison of cavern size and shape between experiments (left half) and simulations (right half) at (a) 50 rpm, (b) 150 rpm, and (c) 300 rpm.

clearly shows that regions with significant fluid motion grow with increasing agitator speed. Particle tracking in the simulated velocity field was compared with the experimental results shown in Figure 14. The tracking simulations were performed by injecting three sets of particles in spherical patterns near each of the impellers and recording their location as they intersected a plane parallel with one of the impellers. For Figure 14, particle tracking results for 50, 150, and 300 rpm were plotted for half of the tank on the right; the left side corresponds to experimental images for the same conditions. These pictures showed that the cavern shapes and sizes were predicted with excellent precision by the CFD simulations using the bounded viscosity model. Furthermore, the lack of communication between caverns was confirmed by color coding the particles. Particles injected near the middle impeller were colored green, and particles injected near the upper and lower impellers were red. No red particles are found in the middle cavern, and, correspondingly, green particles do not enter the upper or lower caverns. These results confirmed that material in each cavern remain separated for a long period of time.

Having a validated model for non-Newtonian fluids is extremely valuable for predicting the behavior of these fluids in larger and/or more complex equipment that cannot be easily validated. Because cavern sizes and non-Newtonian behavior can change on scale-up in manners that cannot be simply correlated to dimensionless numbers, the implementation of validated CFD models may prove to be the most effective way to scale up processes with shear-thinning fluids. CFD also may help in the selection of novel approaches to design scale-down experiments. Simulations could be used to identify experimental fluid properties with similar flow behavior on small scales as in large-scale equipment. The most meaningful experiments for process scale-down may not necessarily use fluids that will have identical physical properties as the final material. With the help of validated CFD simulations, fluid can be selected to recreate in the laboratory the flow patterns that will be formed at large scales. Moreover, the utility of inelastic shear-thinning models in the pharmaceutical industry is not limited to process scale-up. For example, blood is a shear-thinning fluid, and its flow properties are the subject of ongoing computational research (35,36).

Static mixers

The performance of several devices other than stirred tanks can be examined using a combination of CFD and EFD. Static mixers have been studied extensively for a variety of applications (37–39). A primary use is the formulation of liquid–liquid dispersions and emulsions. These mixers consist of flow reorientation devices inserted within a pipe. The shape of the elements depends on the

Figure 15: Four-element SMX mixer.

Table I: Mixing rate as a function of injection location and Reynolds number in an SMX static mixer.

Injection Point	*Re* = 1	*Re* = 30	*Re* = 100
y = 0	0.470	0.468	0.481
y = *R*/2	0.405	0.440	0.447
y = 3*R*/4	0.443	0.430	0.324

manufacturer's designs. One common type of static mixer, a four-element SMX mixer (Sulzer Chemtech USA, LaPorte, TX), is shown in Figure 15. The length-to-diameter of the elements, the number of blades, and the rotation of each element are important geometric parameters. One example of static-mixer use in the pharmaceutical industry is the dispersion of a polymer solution laden with an active pharmaceutical ingredient to form microparticles (40). CFD is an excellent tool for studying flows in static mixers where the complex flow geometry makes visualization experiments difficult and expensive. With a validated model, CFD can be used to design static mixers and predict process performance.

A recent study presented validation and analysis of an SMX static mixer (41). Mixing performance was validated in the computations with a statistical method on the basis of the intensity of segregation concept (42). The method involved following tracer particles that were injected in a segregated initial condition (i.e., a circle at the center of the pipe). As the particles spread through the mixer, the decrease in variation coefficient was computed to quantify mixing. At various mixer cross sections, the area was divided into square boxes or cells of equal size. The number-based standard deviation, σ_N, is shown by

$$\sigma_N = \left(\frac{\sum_{i=1}^{n\text{cells}} (N_i - \bar{N})^2}{n\text{ cells} - 1} \right)^{1/2} \quad [2]$$

in which N_i is the number of particles in box i, $\bar{N}$ is the mean number of particles per cell, and "n cells" is the total number of cells. The relative standard deviation (RSD) was then computed according to the following equation:

$$\text{RSD} = \left(\frac{\sigma_N^2 - \sigma_\infty^2}{\bar{N}^2} \right)^{1/2} \quad [3]$$

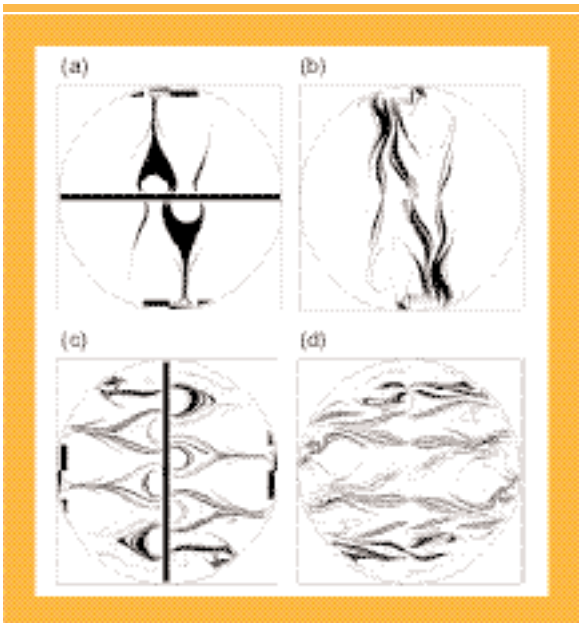

Figure 16: Particle tracking results at *Re* = 1 after 0.5, 1, 1.5, and 2 elements (a–d, respectively).

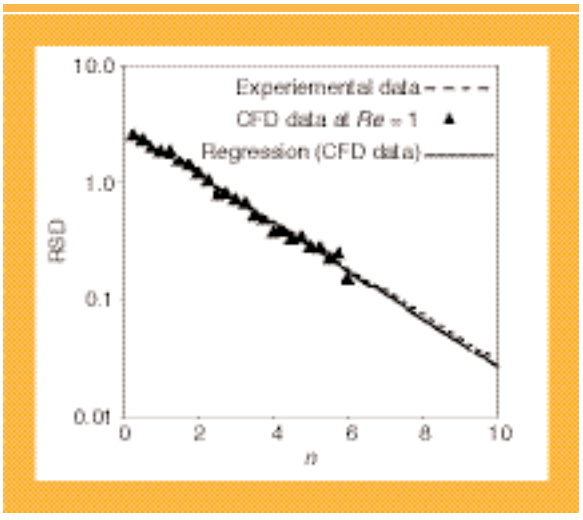

Figure 17: Experimental validation of CFD mixing results.

The residual value of the number-based standard deviation after flow through 10 elements was assigned to σ_∞. Figure 16 shows sample mixing patterns used for these calculations at several downstream locations for particles occupying 10% of the inlet volume at a center of the inlet. The Reynolds number of the flow was chosen as *Re* = 1.0 because experimental RSD data are available at this condition (43). Figure 17 shows that excellent agreement was obtained between the experimental data and the CFD calculations, when RSD was plotted as a function of the number of elements. The mixing rate was equivalent to the slope of these curves on a semilog scale.

The validated CFD model was subsequently used to evaluate mixing rates as a function of injection location for various flow rates or Reynolds numbers. Mixing-rate data were calculated for *Re* = 1, 30, and 100 for three injection locations: the

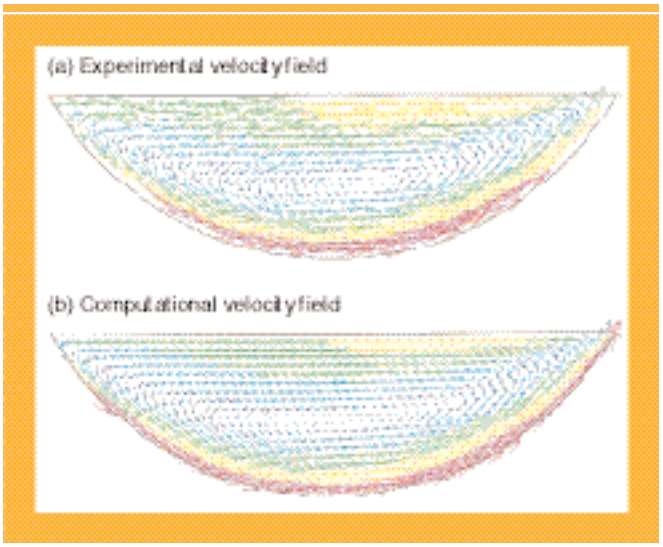

Figure 18: (a) PIV and (b) CFD velocity fields in a roller bottle.

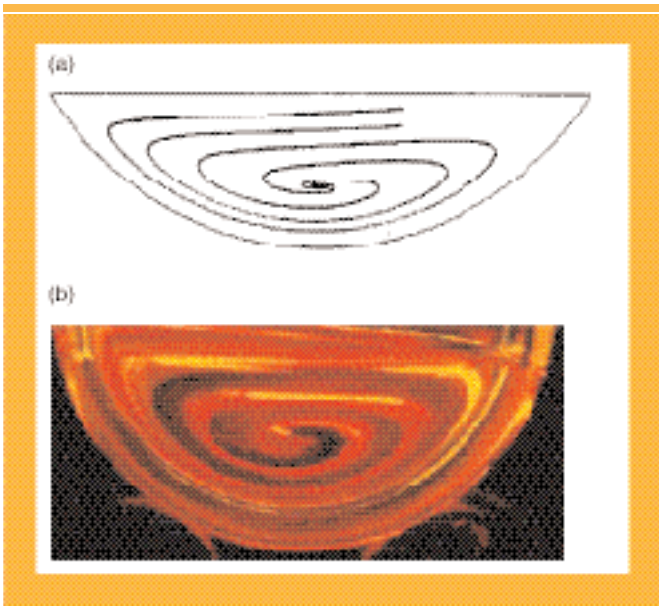

Figure 19: (a) Computational and (b) experimental fluid streamlines in a roller bottle.

center of the pipe ($y = 0$); halfway between the center and outer edge of the pipe ($y = ½$); and three quarters of the way from the center to the edge of the pipe ($y = ¾$) (see Table I). The calculations predicted the fastest mixing rate for injection at the center of the pipe for each *Re* value. The table also indicates that the mixing-rate responses to changes in the Reynolds number are not intuitive and are highly dependent on injection location. Similar to selecting optimal injection location, CFD information can be used to choose optimum mixer length, element aspect ratio, flow rate, and so forth (44,45).

Roller bottles

A final example that demonstrates the diverse applicability of using complementary EFD and CFD comes from a biological system. Roller bottles have been used for more than 40 years in the pharmaceutical and medical fields for processes such as cell growth and infection, vaccine preparation, and plant cell cultivation (46–48). Widespread use of roller bottles can be attributed to several reasons, including the simplicity of the technology. A flow field conducive to biological activity is generated by axially rotating a horizontal cylindrical vessel filled approximately one-fourth of the volume. The system can maintain sterile conditions for a long period of time and allows constant fluid–gas contact and facile addition of nutrients without interruption.

An experimental and computational study of flow in a roller bottle bioreactor characterized mixing in this device for various operating conditions (49,50). Improved mixing can lead to better reactor performance by more evenly distributing cells and nutrients. Figure 18 shows the experimental and computational velocity fields for a cross section at the middle of a moving roller bottle. The results correspond to a 20-cm-long, 10-cm-diameter roller bottle containing water and rotating at a speed of 0.25 rpm. Excellent agreement between the experimental and computational velocity fields is achieved. A good comparison between computational particle tracking and mixing structures identified by LIF techniques also can be shown. Figure 19 shows that the fluid-mixing pattern predicted by CFD (see Figure 19a) also is found experimentally with a PLIF technique (see Figure 19b). The initial condition for these experiments was a vertical line of particles or dye placed at the center of the bottle.

In addition to capturing the motion of the fluid, one must also characterize the behavior of cells and particles that have inertial settling velocities and do not follow the streamlines of the fluid. Figure 20a shows computational streamlines when tracer particles have a settling velocity of $V_S = 0.05U$, in which U is the linear velocity of the wall. An experimental picture of a system with a similar settling rate ($V_S = 0.06U$) in Figure 20b shows a streamline with a comparable trajectory and location. The image was created using long exposure-time photography to capture the pathline followed by a fluorescent particle. Other experiments not described in this article found that particles with an initial location near the liquid surface settled to the bottle wall, results that also were verified by computational results.

The computational model can be used to predict the effect of several modifications, including various rotation speeds, periodic changes in the rotation direction, and various fluid and particle properties. An example is presented in Figure 21, in which the effects of settling velocities of $V_S = 0.02U$, $0.05U$, $0.1U$, and $0.2U$ were examined. For this figure, the settling time distributions were characterized on a gray scale with black zones corresponding to zero residence time and white regions for the maximum computational residence time. Particles that start in the white areas did not settle at all. Analysis showed that only large settling velocities (i.e., $V_S = 0.2U$) allow most cells to reach the bottle walls (49). The relative speed of the bottle wall to the particle settling velocity is clearly shown to have a significant and controllable effect on the distribution of cells in a roller bottle.

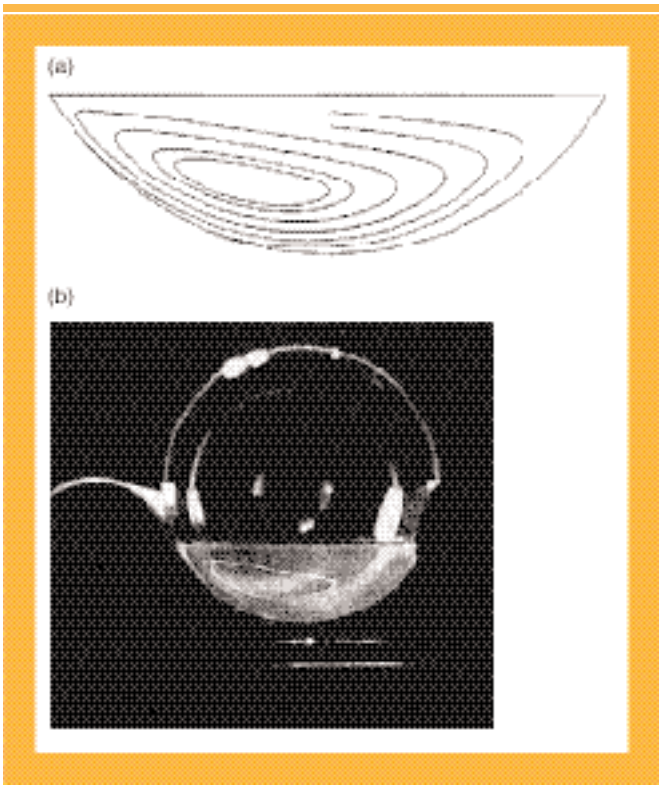

Figure 20: (a) Computational and (b) experimental particle pathlines in a roller bottle.

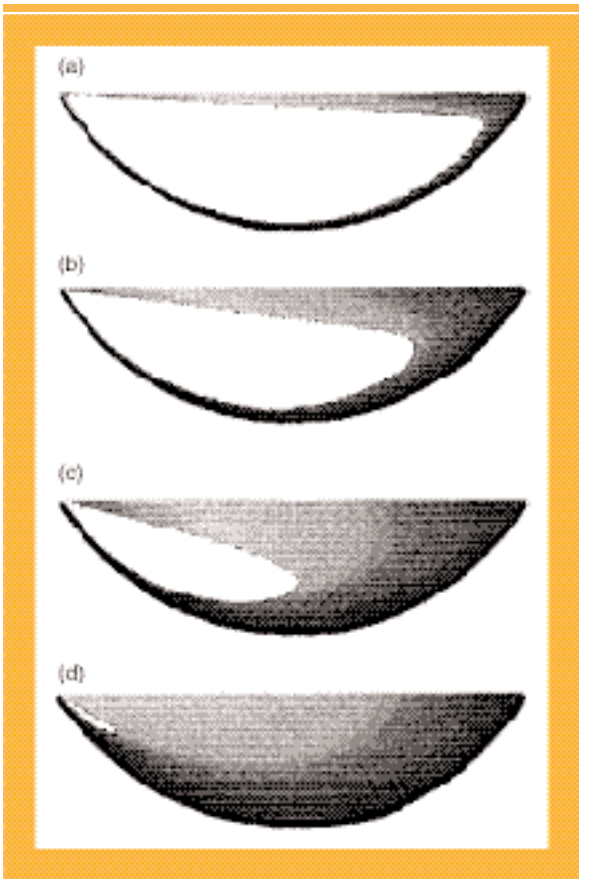

Figure 21: Settling velocity distribution in a roller bottle for $V_s = 0.02U$, $0.05U$, $0.1U$, and $0.2U$ (a–d, respectively) on a gray scale. Black corresponds to zero residence time, and white corresponds to the maximum residence time.

Conclusion

The examples presented in this article are by no means a complete list of all the areas in which experimental and computational fluid dynamics can be useful within the pharmaceutical industry, nor does this article describe all the tools available to perform EFD and CFD. The pharmaceutical industry has many applications that challenge the state of development of techniques at the forefront of EFD and CFD technology. Several gas flows that can be studied with CFD are of considerable interest, ranging from air flow in the lung for aerosol drug delivery to laminar flow in a fume hood for worker safety when handling potent compounds. Many pharmaceutical flows are turbulent and/or involve multiple phases, and much effort is being applied to developing and evaluating turbulent and multiphase CFD models (51–53). The study of these flows will benefit from the combined EFD–CFD approach described in this article. The importance of addressing problems with complementary experimental and computational tools should not be understated. CFD packages are capable of producing output that may "look" correct but are inaccurate for many reasons, including numerical diffusion, inappropriate boundary condition selection, or incorrect physical models within the CFD code. Experimental validation of computations is critical for using CFD appropriately. Despite this limitation, CFD contributes significantly to understanding complex flows by providing data that cannot be easily gathered experimentally.

Advancement of these tools is necessary to expand our understanding of other industrially relevant flows. For example, most slurry systems are opaque and detailed flow information cannot be obtained using visualization based on light. The development of imaging and PIV techniques that use X-rays rather than lasers will allow the characterization of motion in opaque equipment and flow media. Sophisticated PIV data can go beyond confirming the CFD results of complex flows. EFD information also may be used as input for CFD computations for systems in which the physics are not fully described by mathematical models. The pharmaceutical industry and the medical field will benefit from implementing current EFD and CFD technology in many areas as well as from the continued advancement of these tools.

References

1. A. Bakker, A. Haidari, and E. Marshall, "Design Reactors via CFD," *Chem. Eng. Prog.* **97** (12), 30–39 (2001).
2. H.S. Pordal, C.J. Matice, and T.J. Fry, "Computational Fluid Dynamics in the Pharmaceutical Industry," *Pharm. Technol.* **26** (2), 72–79 (2002).
3. J.A. Williams, "Keys to Bioreactor Selections," *Chem. Eng. Prog.* **98** (3), 34–41 (2002).
4. M.R. de Leval et al., "Use of Computational Fluid Dynamics in the Design of Surgical Procedures: Application to the Study of Competitive Flows in Cavopulmonary Connections," *J. Thorac. Cardiovasc. Surg.* **111** (6), 502–513 (1996).
5. L.M. Bocanegra et al., "Fluid and Particle Laser Doppler Velocity Measurements and Mass Transfer Predictions for USP Paddle Method Dissolution Apparatus," *Drug Dev. Ind. Pharm.* **16** (9), 1441–1462 (1990).

6. P.V. Dankwertz, "Continuous Flow Systems: Distribution of Residence Times," *Chem. Eng. Sci.* **2** (1), 1–13 (1953).
7. H.S. Fogler, *Elements of Chemical Reaction Engineering*, Prentice Hall International Series in the Physical and Chemical Engineering Sciences, N. Amundson, Ed. (Prentice Hall, Englewood Cliffs, NJ, 3d ed., 1992), pp. 809–861.
8. B.K. Johnson and R.K. Prud'hommer, "Chemical Processing and Micromixing in Confined Impinging Jets," submitted to *AIChE J.*
9. J. Baldyga, J.R. Bourne, and S.J. Hearn, "Interaction between Chemical Reactions and Mixing on Various Scales," *Chem. Eng. Sci.* **52** (4), 457–466 (1997).
10. J. Baldyga and J.R. Bourne, *Turbulent Mixing and Chemical Reactions* (John Wiley & Sons, Chichester, 1999), pp. 39–47.
11. E.L. Paul and R.E. Treybal, "Mixing and Product Distribution for a Liquid-Phase, Second-Order, Competitive-Consecutive Reaction," *AIChE J.* **17** (3), 718–724 (1971).
12. R.J. Adrian, "Particle Imaging Techniques for Experimental Fluid Mechanics," *Ann. Rev. of Fluid Mech.* **23,** 261–304 (1991).
13. C. Arcoumanis, J.J. McGuirk, and J. Palma, "On the Use of Fluorescent Dyes for Concentration Measurements in Water Flows," *Experiments in Fluids,* **10,** 177–183 (1990).
14. D.R. Unger and F.J. Muzzio, "Laser-Induced Fluorescence Technique for the Quantification of Mixing in Impinging Jets," *AIChE J.* **45** (12), 2477–2485 (1999).
15. D.A. Anderson, J.C. Tannehill, and R.H. Pletcher, *Computational Fluid Mechanics and Heat Transfer* (McGraw-Hill, New York, NY, 1984).
16. G.F. Carey and J.T. Oden, *Finite Elements—Fluid Mechanics, Vol. VI* (Prentice-Hall, Englewood Cliffs, NJ, 1986).
17. F. Shakib and T.J.R. Hughes, "New Finite Element Formulation for Computational Fluid Dynamics IX: Fourier Analysis of Space–Time Galerkin/Least-Squares Algorithms," *Comp. Meth. Applied Mech. Eng.* **87** (1), 35–58 (1991).
18. H. Abdou, "Factors Relating to the Dissolution Apparatus," in *Dissolution, Bioavailability, and Bioequivalence* (Mack Publishing Co., Easton, PA, 1989), pp. 115–143.
19. B. Abrahamsson, K. Roos, and J. Sjogren, "Investigation of Prandial Effects on Hydrophilic Matrix Tablets," *Drug Dev. Ind. Pharm.* **25** (6), 765–771 (1999).
20. W.E. Hamlin et al., "Loss of Sensitivity in Distinguishing Real Differences in Dissolution Rates due to Increasing Intensity of Agitation," *J. of Pharm. Sci.* **51** (5), 432–435 (1962).
21. J. Cartensen, T.Y. Lai, and V.K. Prasad, "USP Dissolution IV: Comparison of Methods," *J. Pharm. Sci.* **67** (9), 1303–1307 (1978).
22. T. Durig and R. Fassihi, "Evaluation of Floating and Sticking Extended Release Delivery Systems: An Unconventional Dissolution Test," *J. Controlled Release* **67** (1), 37–44 (2000).
23. F. Underwood and D. Cadwallader, "Effects of Various Hydrodynamic Conditions on Dissolution Rate Determinations," *J. Pharm. Sci.* **65** (5), 697–700 (1976).
24. C. Wells, "Effect of Sampling Probe Size on Dissolution of Tableted Drug Samples," *J. Pharm. Sci.* **70** (2), 232–233 (1981).
25. J.W. Mauger, "Physiochemical and Mechanical Factors Related to Dissolution Testing," *Dis. Technol.* **3** (1), 7–19 (1996).
26. J. Kukura et al., "Engineering Tools for Understanding Hydrodynamics of Dissolution Tests," accepted for publication by *Drug Dis. Ind. Pharm.*
27. D. Lamberto, M.M. Alvarez, and F.J. Muzzio, "Experimental and Computational Investigation of the Laminar Flow Structure in a Stirred Tank," *Chem. Eng. Sci.* **54** (7), 919–942 (1999).
28. D.J. Lamberto, F.J. Muzzio, and P.D. Swanson, "Using Time-Dependent RPM to Enhance Mixing in Stirred Vessels," *Chem. Eng. Sci.* **51** (5), 733–741 (1996).
29. E.S. Szalai, P. Arratia, and F.J. Muzzio, "Mixing Analysis in a Fermentor Stirred with Ekato Intermig Impellers," submitted to *Biotech Bioengr.*
30. I.P.T. Moore, G. Cossor, and M.R. Baker, "Velocity Distributions in a Stirred Tank Containing a Yield Stress Fluid," *Chem. Eng. Sci.* **50** (15), 2467–2481 (1995).

31. A.B. Metzner and R.E. Otto, "Agitation of Non-Newtonian Fluids," *AIChE J.* **3** (1), 3–10 (1957).
32. P.A. Tanguy, F. Thibault, and E.B. De la Fuente, "A New Investigation of the Metzner-Otto Concept for Anchor Mixing Impellers," *Can. J. Chem. Eng.* **74** (4), 222–228 (1996).
33. E. Galindo and A.W. Nienow, "Mixing of Highly Viscous Simulated Xanthan Fermentation Broths With The Lightnin A-315 Impeller," *Biotech. Prog.* **8** (3), 233–239 (1992).
34. E. Galindo et al., "Comparison of Cavern Developments in Mixing a Yield Stress Fluid by Rushton and Intermig Impellers," *Chem. Eng. Technol.* **19** (4), 315–323 (1996).
35. S. Aluri and K.B. Chandran, "Numerical Simulation of Mechanical Mitral Heart Valve Closure," *Ann. Biomed. Eng.* **29** (8), 665–676 (2001).
36. K. Ryu et al., "Importance of Accurate Geometry in the Study of the Total Cavopulmonary Connection: Computational Simulations and In Vitro Experiments," *Ann. Biomed. Eng.* **29** (10), 844–853 (2001).
37. A. Bakker, "Flow and Mixing with Kenics Static Mixers," *Cray Channels* **15** (3), 25–28 (1993).
38. S.A. Jaffer and E.P. Wood, "Quantification of Laminar Mixing in the Kenics Static Mixer: An Experimental Study," *Can. J. Chem. Eng.* **76** (June), 516–521 (1998).
39. D.M. Hobbs and F.J. Muzzio, "Reynolds Number Effects on Laminar Mixing in the Kenics Static Mixer," *Chem. Eng. J.* **70** (2), 93–104 (1998).
40. M.E. Rickey et al., Preparation of Extended Shelf-Life Biodegradable, Biocompatible Microparticles Containing a Biologically Active Agent, US Patent No. 5,792,477.
41. J.M. Zalc et al., "Characterization of Flow and Mixing in an SMX Static Mixer," *AIChE J.*, **48** (3), 427–436 (2002).
42. P.V. Dankwertz, "The Definition and Measurement of Some Characteristics of Mixtures," *App. Sci. Res.* **3** (Section A), 279–297 (1952).
43. F.A. Streiff, "Adapted Motionless Mixer Design," *Third European Conference on Mixing,* paper C2, 171–188 (1979).
44. D.M. Hobbs and F.J. Muzzio, "Effects of Injection Location, Flow Ratio, and Geometry on Kenics Mixer Performance," *AIchE J.* **43** (12), 3121–3132 (1997).
45. E.S. Szalai and F.J. Muzzio, "A Fundamental Approach to the Design and Optimization of Static Mixers," submitted to *AIChE J.*
46. E.I. Tsao et al., "Optimization of a Roller Bottle Process for the Production of Recombinant Erythropoietin," *Ann. NY Acad. Sci.* **665,** 127–136 (1992).
47. H. Tanaka et al., "Rotating Drum Fermentor for Plant Cell Suspension Cultures," *Biotech. Bioeng.* **25,** 2359–2372 (1983).
48. R. Kunitake et al., "Fully Automated Roller Bottle Handling System for Large-Scale Culture of Mammalian Cells," *J. Biotech.* **52** (3), 289–297 (1997).
49. F.J. Muzzio et al., "Computational and Experimental Investigation of Flow and Particle Settling in a Roller Bottle Bioreactor," *Biotech. Bioeng.* **63** (2), 185–196 (1999).
50. D.R. Unger et al., "Computational and Experimental Investigation of Flow and Fluid Mixing in the Roller Bottle Bioreactor," *Biotech. Bioeng.* **70** (2), 118–130 (2000).
51. S.M. Kresta and P.E. Wood, "Prediction of the Three-Dimensional Turbulent Flow in Stirred Tanks," *AIChE J.* **37** (3), 448–460 (1991).
52. Y.C. Chang et al., "Simulation and Analysis of Cluster Breakage with Applications in Turbulent Mixing," *J. Aerosol Sci.* **20** (8), 895–898 (1989).
53. A. Bakker et al., "The Laminar and Turbulent Flow Pattern of a Pitched Blade Turbine," *T.I. Chem. Eng.-Lond.* **74** (Part A), 485–497 (1996). **PT**